

Fundamental-solution-based hybrid finite element with singularity control for two-dimensional mixed-mode crack problems

Hui Wang^a, Wanqing Lin^a, Qing-Hua Qin^{b,*}

^a College of Civil Engineering & Architecture, Henan University of Technology, Zhengzhou 450001, China

^b Research School of Electrical, Energy and Materials Engineering, Australian National University, Canberra, ACT 2601, Australia

ARTICLE INFO

Keywords:

Stress intensity factor
Crack
Fundamental solutions
Hybrid finite element
Quarter-point singularity

ABSTRACT

In this work, a fundamental-solution-based hybrid finite element method is presented for modeling mixed-mode cracks in two-dimensional (2D) isotropic elastic media. In the method, a double-variable hybrid functional for each element is formulated to derive element stiffness equation in terms of nodal displacements, which includes line integrals along the element boundary only. The element interior displacement field is approximated using a linear combination of displacement fundamental solutions at different source locations, while the independent element frame displacement field is approximated by one-dimensional shape function interpolation. To correctly model the behavior of crack-tip displacement, the discontinuous quarter-point crack-tip singular hybrid element formulation is developed, so that crack tip stress intensity factors can be easily evaluated by the near-tip displacement method. Three numerical examples of internal cracks in 2D elastic domains are presented to show the efficiency of the proposed method.

1. Introduction

Analysis of crack stability and propagation plays a central role in engineering to assess structural safety [1–3] and typically it requires the accurate determination of stress intensity factors (SIFs) [4–6], which in turn relies on the modeling of stress and displacement fields near crack tip. Williams [7] in his original work revealed that the displacement field varies as $r^{1/2}$ in the vicinity of the crack-tip, while the stress and strain fields are $r^{-1/2}$ singular at the crack tip, where r is the radial distance from the crack tip, which is measured in the local coordinates (\hat{x}_1, \hat{x}_2) defined at the crack tip, as depicted in Fig. 1.

Usually, in order to represent the complex displacements and stresses in the vicinity of crack tip, simulation technologies using some numerical methods such as finite element methods (FEM) [8,9] and boundary element methods (BEM) [10,11] have to be employed. However, the conventional interpolating polynomials don't contain the terms related to the $r^{1/2}$ and $r^{-1/2}$ variations of crack-tip displacements and stresses. Thus, the singularity of stresses cannot be reflected by the interpolating polynomials, although the displacements can be adequately modelled by refined meshes around the crack tip [12]. To overcome this, the isoparametric quarter-point elements have been defined by placing the midpoint node at the quarter point for the implementation of FEM [13–15] and BEM [16–19]. These works showed that the quarter-point elements have the capability to model exactly inverse square-root singu-

larity of the stresses near the crack tip. However, the accuracy of results is strongly related to the mesh density, especially in FEM, although the FEM can conveniently achieve the domain element discretization for a specific complex mechanical problem. In contrast to the FEM, the BEM uses the boundary integral equation to reduce computational time. But it is difficult to deal with problems including multiple subdomains, because extra equations are required to enforce the continuity of adjacent subdomains.

This paper presents an alternative simulation strategy for modeling 2D cracks and subsequent SIF computation. The essence of the present approach is a mesh discretization of cracked domain using n -sided ($n \geq 3$) hybrid finite elements which utilize a complete set of fundamental solutions of the governing partial differential equations originated at different source points as basis functions for approximating element interior displacement and stress fields [20], instead of T-complete solutions in Trefftz finite element [21–24]. Along the element boundary, the standard isoparametric quadratic approximation is assumed for the element frame displacement. To capture the stress singular behavior in the vicinity of crack tip, the quarter-point singular interpolation along element boundary is employed. The present hybrid finite element formulation can be regarded as the combination of FEM and BEM and has some inherent advantages: (1) the quality of results is element size independent and is strongly related to the element interior interpolation mode [25], (2) only integration along the element boundary has to be carried

* Corresponding author.

E-mail address: qinghua.qin@anu.edu.au (Q.-H. Qin).

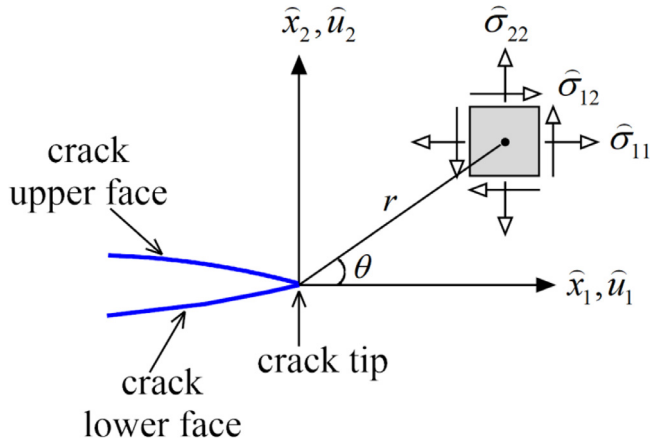


Fig. 1. Schematics of coordinate system at crack tip.

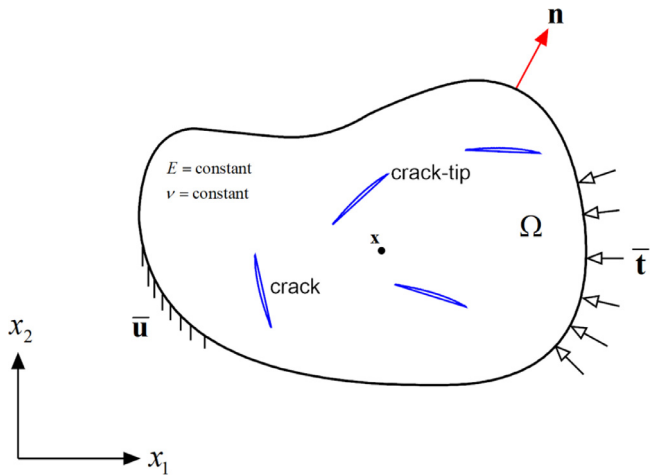


Fig. 2. Schematic of a finite domain containing internal cracks.

out, which allows the use of standard quadrature rules, and thus effectively reduces the dimension of the calculation by one [25,26], (3) arbitrary n -sided elements are allowed for domain discretization [27,28], (3) unified basis functions are employed for field interpolation in all n -sided elements, rather than that in FEM, (4) in special cases the fundamental solutions can fulfill boundary conditions of defects as well so that hybrid superelements, i.e. super hole element [20], super discontinuous load element [29], super graded element [30], super fiber element [31], etc., can be constructed to enclose defects so that the meshing and computing efforts around defects can be simplified.

The paper is arranged as follows. The mathematical formulation of the problem is given in Section 2. The hybrid finite element formulation and its crack implementation are presented in Section 3. The computation of SIFs is described in Section 4. Numerical results are presented in Section 5 and finally some conclusions are drawn in Section 6.

2. Problem statement

Consider an isotropic homogeneous 2D elastic domain which contains several internal cracks, as shown in Fig. 2, in which the crack is defined in terms of upper and lower faces Γ_c^+ and Γ_c^- , respectively. The two crack faces are geometrically coincident, i.e. the normal vectors satisfy $\mathbf{n}_c^+ = -\mathbf{n}_c^-$ where \mathbf{n}_c^+ and \mathbf{n}_c^- are the normals to Γ_c^+ and Γ_c^- , respectively, as indicated in Fig. 3. It is also assumed that the crack faces are free of external forces.

With the assumption that the domain is free of body forces, the equilibrium equations in the standard Cartesian coordinates (x_1, x_2) can be

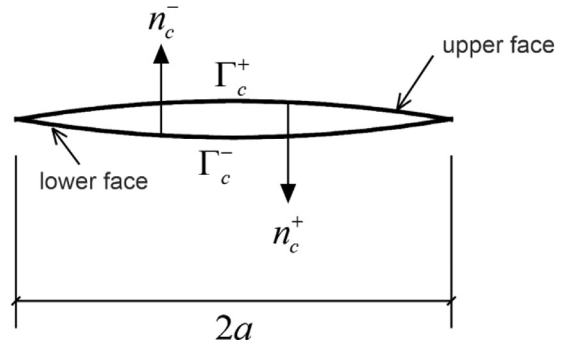


Fig. 3. Schematic of an internal crack.

written as

$$\mathbf{L}^T \boldsymbol{\sigma}(\mathbf{x}) = \mathbf{0} \quad (1)$$

where $\boldsymbol{\sigma}(\mathbf{x}) = [\sigma_{11}(\mathbf{x}) \quad \sigma_{22}(\mathbf{x}) \quad \sigma_{12}(\mathbf{x})]^T$ is stress vector consisting of stress components σ_{ij} ($i, j = 1, 2$) at a point \mathbf{x} and \mathbf{L} is the partial derivative operator matrix

$$\mathbf{L} = \begin{bmatrix} \frac{\partial}{\partial x_1} & 0 \\ 0 & \frac{\partial}{\partial x_2} \\ \frac{\partial}{\partial x_2} & \frac{\partial}{\partial x_1} \end{bmatrix} \quad (2)$$

With the small deformation approximation, the strain can be given by displacement derivatives to the spatial variable

$$\boldsymbol{\varepsilon}(\mathbf{x}) = \mathbf{L}\mathbf{u}(\mathbf{x}) \quad (3)$$

where $\boldsymbol{\varepsilon}(\mathbf{x}) = [\varepsilon_{11}(\mathbf{x}) \quad \varepsilon_{22}(\mathbf{x}) \quad \gamma_{12}(\mathbf{x})]^T$ is the strain vector and $\mathbf{u}(\mathbf{x}) = [u_1(\mathbf{x}) \quad u_2(\mathbf{x})]^T$ is displacement vector.

In the linear elastic theory for isotropic homogeneous material, the stress $\boldsymbol{\sigma}$ connects to the strain $\boldsymbol{\varepsilon}$ through a constant material matrix related to Young's modulus E and Poisson's ratio ν

$$\boldsymbol{\sigma}(\mathbf{x}) = \mathbf{c}\boldsymbol{\varepsilon}(\mathbf{x}) \quad (4)$$

in which

$$\mathbf{c} = \frac{E}{(1+\nu)(1-2\nu)} \begin{bmatrix} 1-\nu & \nu & 0 \\ \nu & 1-\nu & 0 \\ 0 & 0 & \frac{1-2\nu}{2} \end{bmatrix} \quad (\text{plane strain}) \quad (5)$$

or

$$\mathbf{c} = \frac{E}{(1+\nu)(1-\nu)} \begin{bmatrix} 1 & \nu & 0 \\ \nu & 1 & 0 \\ 0 & 0 & \frac{1-\nu}{2} \end{bmatrix} \quad (\text{plane stress}) \quad (6)$$

Besides, the displacement $\bar{\mathbf{u}}$ and traction $\bar{\mathbf{t}}$ are prescribed on the outer boundary portions Γ_u and Γ_t , respectively, that is

$$\begin{aligned} \mathbf{u} &= \bar{\mathbf{u}}, & \text{on } \Gamma_u \\ \mathbf{t} &= \bar{\mathbf{t}}, & \text{on } \Gamma_t \end{aligned} \quad (7)$$

where the boundary traction $\mathbf{t} = [t_1 \quad t_2]^T$ connects to the stresses by the expression

$$\mathbf{t} = \mathbf{A}\boldsymbol{\sigma} \quad (8)$$

in which

$$\mathbf{A} = \begin{bmatrix} n_1 & 0 & n_2 \\ 0 & n_2 & n_1 \end{bmatrix} \quad (9)$$

n_i is the i th component of the unit outward normal \mathbf{n} to the outer boundary Γ_o , and $\Gamma_u \cup \Gamma_t = \Gamma_o$, $\Gamma_u \cap \Gamma_t = \emptyset$.

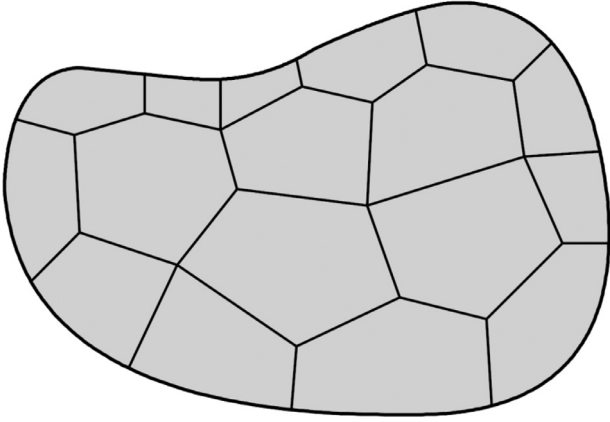


Fig. 4. Schematics of domain discretization by n -sided polygonal elements.

3. Hybrid element formulation

In the computation, the elastic solid with complex geometries is firstly divided into a number of n -sided polygonal elements ($n \geq 3$). Fig. 4 shows an example of a polygonal mesh for a 2D solid, and it is seen that it is possible for the computing domain to consist of different types of polygonal elements with different numbers of edges, as long as they are geometrical compatible (no gaps and overlapping) on the boundaries between adjacent elements. Once the domain discretization is finished, we can introduce unified displacement approximations for all polygonal elements. As an example, let's consider a typical polygonal element shown in Fig. 5. It is assumed that the whole element domain consists of the interior domain Ω_e and the boundary Γ_e . In the present hybrid finite element formulation, different patterns of the displacement field on the boundary and in the interior domain are respectively introduced.

3.1. Intra-element displacement field

Within the interior of element, the displacement field at arbitrary field point \mathbf{x} is approximated by a linear combination of fundamental solutions centered at series of source points \mathbf{x}_{si} ($i=1, 2, \dots, m$) locating outside the element domain ($\mathbf{x}_{si} \notin \Omega_e$), that is,

$$\mathbf{u}(\mathbf{x}) = \mathbf{N}_e(\mathbf{x})\mathbf{c}_e, \quad \mathbf{x} \in \Omega_e \quad (10)$$

where $\mathbf{c}_e = [\mathbf{c}_1^T \quad \mathbf{c}_2^T \quad \dots \quad \mathbf{c}_m^T]^T$ is an unknown coefficient vector (not nodal displacement value) with size $2 \times m$, and $\mathbf{c}_i^T = [c_{1i} \quad c_{2i}]$. The displacement kernel matrix

$$\mathbf{N}_e(\mathbf{x}) = [\mathbf{N}_1(\mathbf{x}) \quad \mathbf{N}_2(\mathbf{x}) \quad \dots \quad \mathbf{N}_m(\mathbf{x})] \quad (11)$$

with

$$\mathbf{N}_i(\mathbf{x}) = \begin{bmatrix} U_{11}^*(\mathbf{x}, \mathbf{x}_{si}) & U_{21}^*(\mathbf{x}, \mathbf{x}_{si}) \\ U_{12}^*(\mathbf{x}, \mathbf{x}_{si}) & U_{22}^*(\mathbf{x}, \mathbf{x}_{si}) \end{bmatrix}, \quad i = 1, 2, \dots, m \quad (12)$$

in which the fundamental solution $U_{lk}^*(\mathbf{x}, \mathbf{x}_s)$ is the induced displacement component at point \mathbf{x} caused by the l -direction unit force at the source point \mathbf{x}_s and can be expressed as [10]

$$U_{lk}^*(\mathbf{x}, \mathbf{x}_s) = \frac{1}{8\pi G(1-\nu)} \left[(3-4\nu)\delta_{lk} \ln \frac{1}{r} + \frac{\partial r}{\partial x_l} \frac{\partial r}{\partial x_k} \right], \quad l, k = 1, 2 \quad (13)$$

In Eq. (13), $r = \sqrt{r_k r_k}$ with $r_k = x_k - x_{sk}$, δ_{lk} denotes the Dirac function, and $G = E/2/(1+\nu)$ is the shear modulus.

Generally, the locations of source points outside the element domain can be pre-assigned to simplify the computing procedure (see Fig. 6), and in the present formulation, the locations of these source points are chosen at a *pseudo* boundary which is geometrically similar to the actual element boundary Γ_e by

$$\mathbf{x}_s = \mathbf{x}_b + \gamma(\mathbf{x}_b - \mathbf{x}_c) \quad (14)$$

where \mathbf{x}_s , \mathbf{x}_b , and \mathbf{x}_c represent the coordinates of source point, boundary point and centroid of the element, respectively. $\gamma > 0$ is a dimensionless parameter controlling the distance of source point to the element boundary [32]. Besides, for the sake of simplicity, the number of source points outside the domain can be chosen to be same as that of nodes in practical computation.

Correspondingly, the stress field can be obtained by substituting Eq. (10) into the governing Eqs. (3) and (4)

$$\boldsymbol{\sigma}(\mathbf{x}) = \mathbf{S}_e(\mathbf{x})\mathbf{c}_e \quad (15)$$

where

$$\mathbf{S}_e(\mathbf{x}) = [\mathbf{S}_1(\mathbf{x}) \quad \mathbf{S}_2(\mathbf{x}) \quad \dots \quad \mathbf{S}_m(\mathbf{x})] \quad (16)$$

with

$$\mathbf{S}_i(\mathbf{x}) = \begin{bmatrix} S_{111}^*(\mathbf{x}, \mathbf{x}_{si}) & S_{211}^*(\mathbf{x}, \mathbf{x}_{si}) \\ S_{122}^*(\mathbf{x}, \mathbf{x}_{si}) & S_{222}^*(\mathbf{x}, \mathbf{x}_{si}) \\ S_{112}^*(\mathbf{x}, \mathbf{x}_{si}) & S_{212}^*(\mathbf{x}, \mathbf{x}_{si}) \end{bmatrix}, \quad i = 1, 2, \dots, m \quad (17)$$

in which the fundamental solution $S_{lkj}^*(\mathbf{x}, \mathbf{x}_s)$ is the induced stress component at point \mathbf{x} caused by the l -direction unit force at the source point \mathbf{x}_s [10]

$$S_{lkj}^*(\mathbf{x}, \mathbf{x}_s) = \frac{1}{4\pi(1-\nu)r} \left[(1-2\nu) \left(\frac{\partial r}{\partial x_l} \delta_{kj} - \frac{\partial r}{\partial x_j} \delta_{kl} - \frac{\partial r}{\partial x_k} \delta_{jl} \right) - 2 \frac{\partial r}{\partial x_l} \frac{\partial r}{\partial x_k} \frac{\partial r}{\partial x_j} \right], \quad l, k, j = 1, 2 \quad (18)$$

Then, the caused traction distribution on the element boundary can be given by

$$\mathbf{t}(\mathbf{x}) = \mathbf{Q}_e(\mathbf{x})\mathbf{c}_e \quad (19)$$

where

$$\mathbf{Q}_e(\mathbf{x}) = \mathbf{A}\mathbf{S}_e(\mathbf{x}) \quad (20)$$

3.2. Element frame displacement field

Although the intra-element fields developed above satisfy the governing equations of elasticity, the continuity requirement of the displacements on the common interface from the adjacent elements is not taken into consideration. In order to enforce such conformity, the displacement field $\tilde{\mathbf{u}}$ defined along the element boundary Γ_e can be written as

$$\tilde{\mathbf{u}}(\mathbf{x}) = \tilde{\mathbf{N}}_e \mathbf{d}_e, \quad \mathbf{x} \in \Gamma_e \quad (21)$$

where $\tilde{\mathbf{N}}_e$ denotes the interpolation matrix relating the element boundary displacement $\tilde{\mathbf{u}}$ to the nodal displacement vector \mathbf{d}_e , and

$$\tilde{\mathbf{N}}_e = [\tilde{\mathbf{N}}_1 \quad \tilde{\mathbf{N}}_2 \quad \dots \quad \tilde{\mathbf{N}}_p] \quad (22)$$

$$\mathbf{d}_e = [\mathbf{d}_1 \quad \mathbf{d}_2 \quad \dots \quad \mathbf{d}_p]^T \quad (23)$$

For the n -sided element with n edges and p nodes, if there are three nodes on each edge for crack simulation, we have $p = 2n$. For such case, the isoparametric quadratic interpolation scheme has to be employed. For example, when the boundary point \mathbf{x} locates on the i th edge ($i = 1, 2, \dots, n-1$),

$$\tilde{\mathbf{N}}_{2i-1} = \begin{bmatrix} \tilde{N}_1(\xi) & 0 \\ 0 & \tilde{N}_1(\xi) \end{bmatrix}, \tilde{\mathbf{N}}_{2i} = \begin{bmatrix} \tilde{N}_2(\xi) & 0 \\ 0 & \tilde{N}_2(\xi) \end{bmatrix}, \tilde{\mathbf{N}}_{2i+1} = \begin{bmatrix} \tilde{N}_3(\xi) & 0 \\ 0 & \tilde{N}_3(\xi) \end{bmatrix}, \tilde{\mathbf{N}}_j = \begin{bmatrix} 0 & 0 \\ 0 & 0 \end{bmatrix} \quad (j \neq 2i-1, 2i, 2i+1) \quad (24)$$

in which \tilde{N}_i ($i=1,2,3$) stands for the standard shape functions in terms of natural coordinate $\xi \in [-1, 1]$ as defined in Fig. 7 and can be found in most of textbooks on finite/boundary element methods [8,10], i.e.

$$\tilde{N}_1 = -\frac{\xi(1-\xi)}{2}, \tilde{N}_2 = 1-\xi^2, \tilde{N}_3 = \frac{\xi(1+\xi)}{2} \quad (25)$$

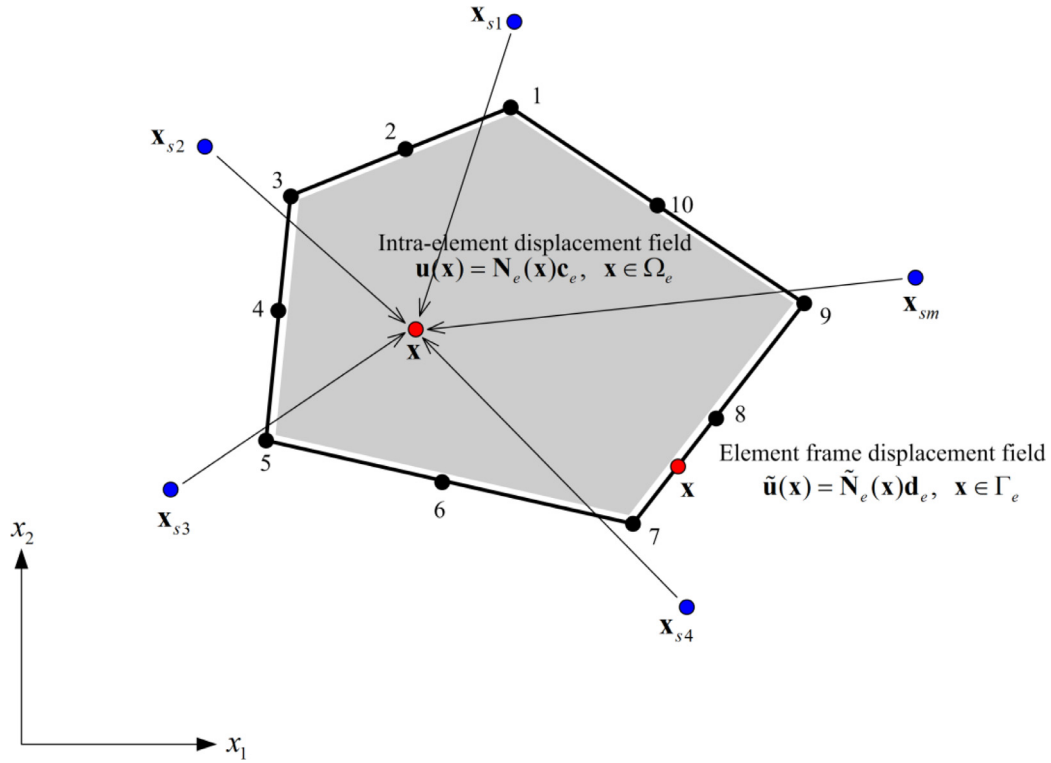


Fig. 5. Displacement approximations for hybrid finite element.

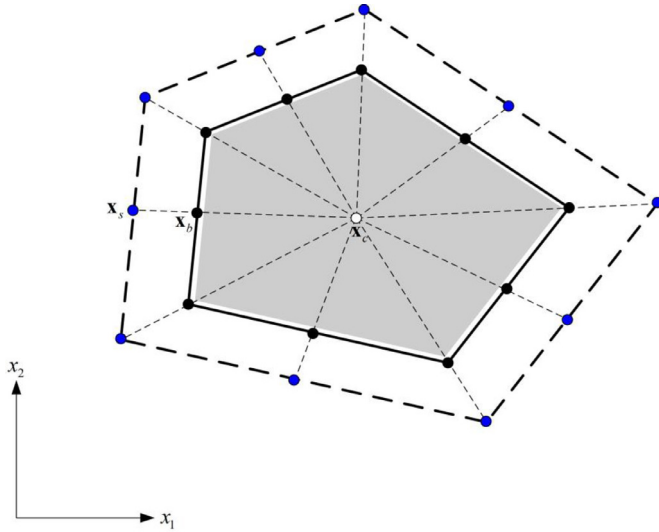


Fig. 6. Schematics of location and quantity of source points.

Specially, when the point \mathbf{x} locates on the n th edge,

$$\begin{aligned} \tilde{\mathbf{N}}_{2n-1} &= \begin{bmatrix} \tilde{N}_1(\xi) & 0 \\ 0 & \tilde{N}_1(\xi) \end{bmatrix}, \tilde{\mathbf{N}}_{2n} = \begin{bmatrix} \tilde{N}_2(\xi) & 0 \\ 0 & \tilde{N}_2(\xi) \end{bmatrix}, \\ \tilde{\mathbf{N}}_1 &= \begin{bmatrix} \tilde{N}_3(\xi) & 0 \\ 0 & \tilde{N}_3(\xi) \end{bmatrix}, \tilde{\mathbf{N}}_j = \begin{bmatrix} 0 & 0 \\ 0 & 0 \end{bmatrix} \quad (j \neq 2n-1, 2n, 1) \end{aligned} \quad (26)$$

Simultaneously, for the isoparametric quadratic boundary of interest, the Cartesian coordinate \mathbf{x} is also related to the natural coordinate ξ , as indicated in Fig. 8, in a parametric form

$$\mathbf{x}(\xi) = \tilde{\mathbf{N}}_e \delta_e, \quad \mathbf{x} \in \Gamma_e \quad (27)$$

where $\delta_e = [x_1 \quad x_2 \quad \cdots \quad x_p]^T$ is the vector consisting of nodal coordinates $x_i (i = 1, 2, \dots, p)$.

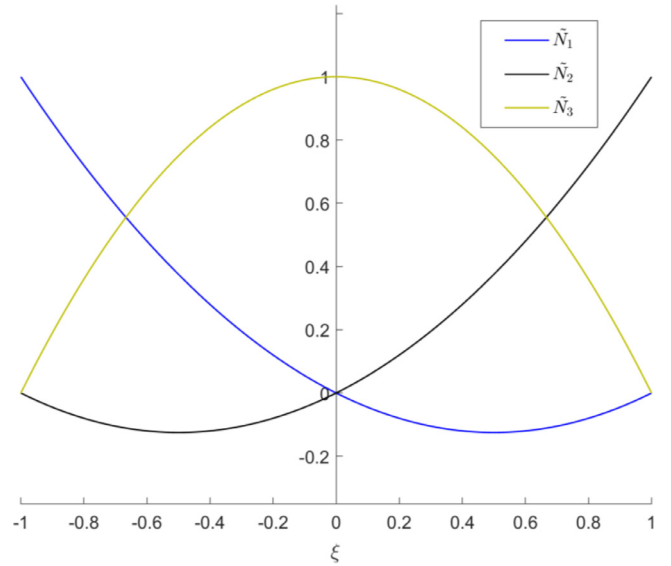


Fig. 7. Shape functions for geometric and displacement approximation along element edge.

3.3. Extended potential

Having the independently defined intra-element displacement field and element frame displacement field for a particular element e , the following hybrid functional Π_{me} is defined to establish a link between the two types of fields associated with the element e [20,33]

$$\Pi_{me} = \frac{1}{2} \int_{\Omega_e} \boldsymbol{\sigma}^T \boldsymbol{\epsilon} d\Omega - \int_{\Gamma_e^t} \bar{\mathbf{t}}^T \bar{\mathbf{u}} d\Gamma + \int_{\Gamma_e} \mathbf{t}^T (\bar{\mathbf{u}} - \mathbf{u}) d\Gamma \quad (28)$$

where $\Gamma_e^t = \Gamma_e \cap \Gamma_e^t$ represents the element traction boundary.

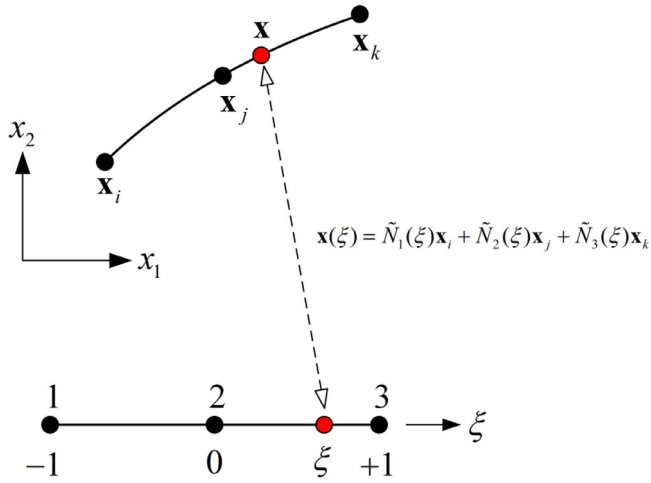


Fig. 8. Geometric interpolation on a specific edge.

Performing integration by parts of Eq. (28) and then applying the Gaussian theorem to it result in

$$\Pi_{me} = \frac{1}{2} \left[\int_{\Gamma_e} \mathbf{t}^T \mathbf{u} d\Gamma - \int_{\Omega_e} (\mathbf{L}^T \boldsymbol{\sigma})^T \mathbf{u} d\Omega \right] - \int_{\Gamma_e'} \bar{\mathbf{t}}^T \bar{\mathbf{u}} d\Gamma + \int_{\Gamma_e} \mathbf{t}^T (\bar{\mathbf{u}} - \mathbf{u}) d\Gamma \quad (29)$$

The intra-element displacement field satisfies the governing equations of elasticity and therefore the domain integration in Eq. (29) vanishes. The remaining terms are

$$\Pi_{me} = -\frac{1}{2} \int_{\Gamma_e} \mathbf{t}^T \mathbf{u} d\Gamma - \int_{\Gamma_e'} \bar{\mathbf{t}}^T \bar{\mathbf{u}} d\Gamma + \int_{\Gamma_e} \mathbf{t}^T \bar{\mathbf{u}} d\Gamma \quad (30)$$

Substituting Eqs. (10), (19) and (21) into Eq. (30), the hybrid functional (30) is rewritten in terms of the undetermined coefficient \mathbf{c}_e and the nodal displacement \mathbf{d}_e as

$$\Pi_{me} = -\frac{1}{2} \mathbf{c}_e^T \mathbf{H}_e \mathbf{c}_e - \mathbf{d}_e^T \mathbf{g}_e + \mathbf{c}_e^T \mathbf{G}_e \mathbf{d}_e \quad (31)$$

with

$$\begin{aligned} \mathbf{H}_e &= \int_{\Gamma_e} \mathbf{Q}_e^T \mathbf{N}_e \mathbf{d}\Gamma \\ \mathbf{G}_e &= \int_{\Gamma_e} \mathbf{Q}_e^T \tilde{\mathbf{N}}_e \mathbf{d}\Gamma \\ \mathbf{g}_e &= \int_{\Gamma_e'} \tilde{\mathbf{N}}_e^T \bar{\mathbf{t}} \mathbf{d}\Gamma \end{aligned} \quad (32)$$

which can be further converted into integrals related to the single variable ξ , that is

$$\begin{aligned} \mathbf{H}_e &= \int_{-1}^1 \mathbf{Q}_e^T \mathbf{N}_e J_\Gamma(\xi) d\xi \\ \mathbf{G}_e &= \int_{-1}^1 \mathbf{Q}_e^T \tilde{\mathbf{N}}_e J_\Gamma(\xi) d\xi \\ \mathbf{g}_e &= \int_{-1}^1 \tilde{\mathbf{N}}_e^T \bar{\mathbf{t}} J_\Gamma(\xi) d\xi \end{aligned} \quad (33)$$

In Eq. (33), $J_\Gamma(\xi)$ is the boundary Jacobian, which can be evaluated by the transformation Eq. (27) of \mathbf{x} and ξ , i.e.

$$J_\Gamma(\xi) = \sqrt{\left(\frac{\partial x_1}{\partial \xi} \right)^2 + \left(\frac{\partial x_2}{\partial \xi} \right)^2} \quad (34)$$

The stationary value of Π_{me} in Eq. (31) with respect to \mathbf{c}_e and \mathbf{d}_e yields the following relations

$$\begin{aligned} \frac{\partial \Pi_{me}}{\partial \mathbf{c}_e^T} &= -\mathbf{H}_e \mathbf{c}_e + \mathbf{G}_e \mathbf{d}_e = \mathbf{0} \\ \frac{\partial \Pi_{me}}{\partial \mathbf{d}_e^T} &= \mathbf{G}_e^T \mathbf{c}_e - \mathbf{g}_e = \mathbf{0} \end{aligned} \quad (35)$$

from which the optional relationship between \mathbf{c}_e and \mathbf{d}_e , and the element stiffness equation can be respectively given by

$$\mathbf{c}_e = \mathbf{H}_e^{-1} \mathbf{G}_e \mathbf{d}_e \quad (36)$$

$$\mathbf{K}_e \mathbf{d}_e = \mathbf{g}_e \quad (37)$$

where

$$\mathbf{K}_e = \mathbf{G}_e^T \mathbf{H}_e^{-1} \mathbf{G}_e \quad (38)$$

is the element stiffness matrix, which keeps symmetric in practice.

Assembling symmetric element stiffness matrix for each element and imposing the specific displacement constraints lead to an algebraic system of equations, which can be solved for determining the nodal displacements. This procedure is the same as that in the traditional finite element method [8,34]. Subsequently, the coefficient \mathbf{c}_e can be evaluated by Eq. (36). Then the displacements and stresses at any point in the element can be evaluated by Eqs. (10) and (15).

4. Calculation of stress intensity factors

The task of interest in fracture analysis is the calculation of stress intensity factors which are local parameters to determine whether the cracks propagate. The most common methods for evaluating the SIFs are the J-integral method and the near-tip displacement method [35–37]. The latter is much preferred in practice since the displacement calculation in most of numerical methods is straight forward and requires very little calculation [12,16,17], and hence the near tip displacement method is employed in this study to evaluate the SIFs for mixed-mode crack problems.

As depicted in Fig. 1, the near-tip displacement fields \hat{u}_1 and \hat{u}_2 at point (r, θ) in the local coordinates (\hat{x}_1, \hat{x}_2) are related to stress intensity factors $K_{I,II}$ and can be written as [4,7]

$$\begin{aligned} \hat{u}_1 &= \frac{K_I}{4\mu} \sqrt{\frac{r}{2\pi}} \left[(2\kappa - 1) \cos \frac{\theta}{2} - \cos \frac{3\theta}{2} \right] \\ &\quad + \frac{K_{II}}{4\mu} \sqrt{\frac{r}{2\pi}} \left[(2\kappa + 3) \sin \frac{\theta}{2} + \sin \frac{3\theta}{2} \right] + O(r) \\ \hat{u}_2 &= \frac{K_I}{4\mu} \sqrt{\frac{r}{2\pi}} \left[(2\kappa + 1) \sin \frac{\theta}{2} - \sin \frac{3\theta}{2} \right] \\ &\quad - \frac{K_{II}}{4\mu} \sqrt{\frac{r}{2\pi}} \left[(2\kappa - 3) \cos \frac{\theta}{2} + \cos \frac{3\theta}{2} \right] + O(r) \end{aligned} \quad (39)$$

where $\mu = E/2/(1 + \nu)$ is shear modulus, $\kappa = 3 - 4\nu$ for plane strain and $\kappa = (3 - \nu)/(1 + \nu)$ for plane stress.

Specially, when $\theta = \pm\pi$, that is, the point locates on the upper and lower faces, the relative normal displacement Δu_n and tangential displacement Δu_t at r (see Fig. 9) can be given by

$$\begin{aligned} \Delta u_n &= \hat{u}_2(r, \pi) - \hat{u}_2(r, -\pi) = \frac{K_I}{\mu} \sqrt{\frac{r}{2\pi}} (\kappa + 1) \\ \Delta u_t &= \hat{u}_1(r, \pi) - \hat{u}_1(r, -\pi) = \frac{K_{II}}{\mu} \sqrt{\frac{r}{2\pi}} (\kappa + 1) \end{aligned} \quad (40)$$

from which the stress intensity factors $K_{I,II}$ can be calculated as

$$\begin{aligned} K_I &= \frac{\mu}{1 + \kappa} \sqrt{\frac{2\pi}{r}} \Delta u_n \\ K_{II} &= \frac{\mu}{1 + \kappa} \sqrt{\frac{2\pi}{r}} \Delta u_t \end{aligned} \quad (41)$$

Moreover, because the near-tip displacements are normally evaluated in the global coordinates (x_1, x_2) for the implementation of the present hybrid finite element method, the displacement transformation is needed for the case of inclined crack, as displayed in Fig. 10. If the

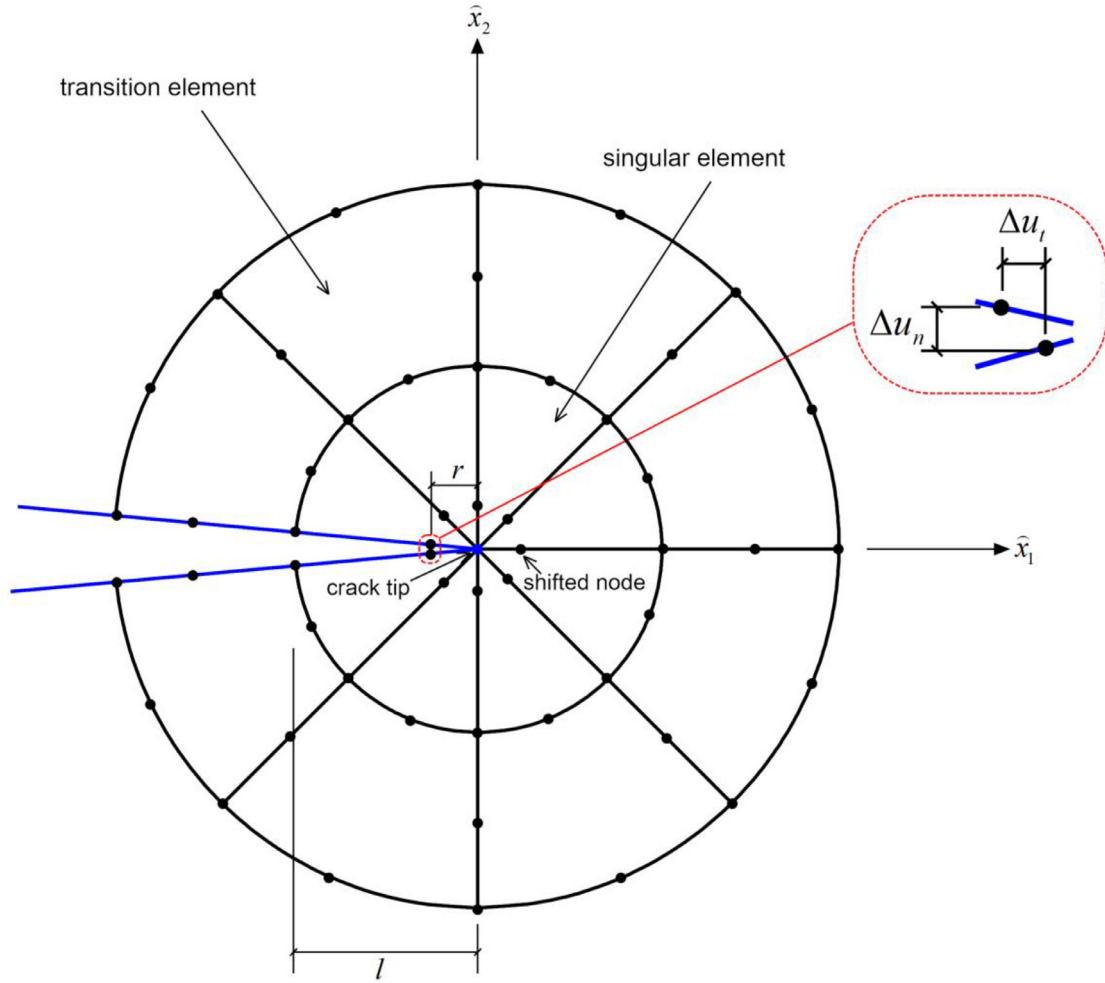


Fig. 9. Singular quarter-point elements at crack tip.

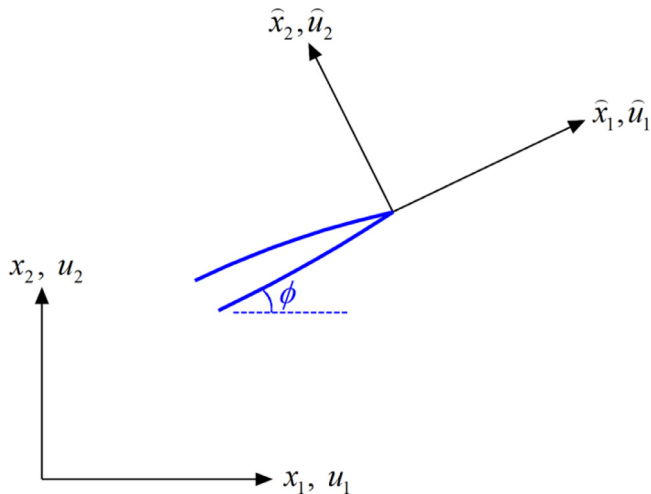


Fig. 10. Correlation between the global and local coordinates for inclined crack problem.

angle of crack inclination is represented by ϕ , the correlation between the global and local displacements can be written as

$$\begin{bmatrix} \hat{u}_1 \\ \hat{u}_2 \end{bmatrix} = \begin{bmatrix} \cos \phi & \sin \phi \\ -\sin \phi & \cos \phi \end{bmatrix} \begin{bmatrix} u_1 \\ u_2 \end{bmatrix} \quad (42)$$

Obviously, the accuracy of the SIFs depends on the quality of representation of the asymptotic displacement and stress fields. To capture the $\mathbf{u} \sim r^{1/2}$ displacement behavior and the $\sigma \sim r^{-1/2}$ stress behavior in the vicinity of the crack tip, the singular quarter-point crack-tip element is employed in this work. This singular quarter-point crack-tip element can be achieved by using three-node edges with midside nodes shifted from central positions to quarter-side positions [14,38], as indicated in Fig. 9. The length l of the quarter-point element at crack-tip (see Fig. 9) is generally assumed to be $l/a = 1/10$ in the practical computation, according to the suggestion of Blandford et.al. [18], where a is the half crack length. For such singular controlling case, the displacement and geometric approximations expressed by the shape functions in Eq. (25) along an element edge, i.e. consisting of nodes i, j, k , can be found in Fig. 11. Besides, the general 4-sided transition elements are allocated around the singular 3-sided elements to achieve regular mesh configuration in the near-tip region over which the crack is sensed.

5. Numerical results and discussion

To demonstrate the accuracy and efficiency of the proposed formulation, three numerical examples have been taken into consideration to evaluate stress intensity factors, involving the centered crack, inclined crack and two inclined cracks. Moreover, in all cases, finite plate is subjected to a uniform tension in one direction.

5.1. A central crack in a finite plate

The first example is a finite plate with a central crack under uniform tension $\sigma_0 = 30$ MPa perpendicular to the crack line (Fig. 12). The

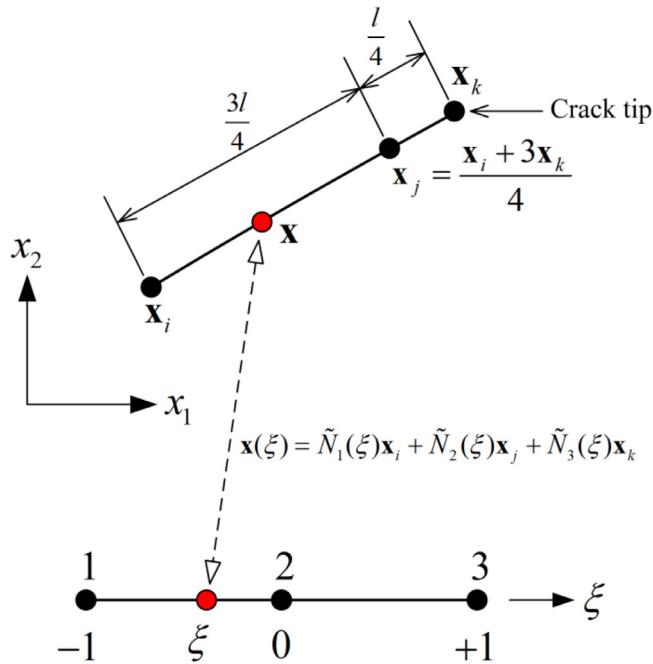


Fig. 11. Singular quarter-point approximation near crack tip.

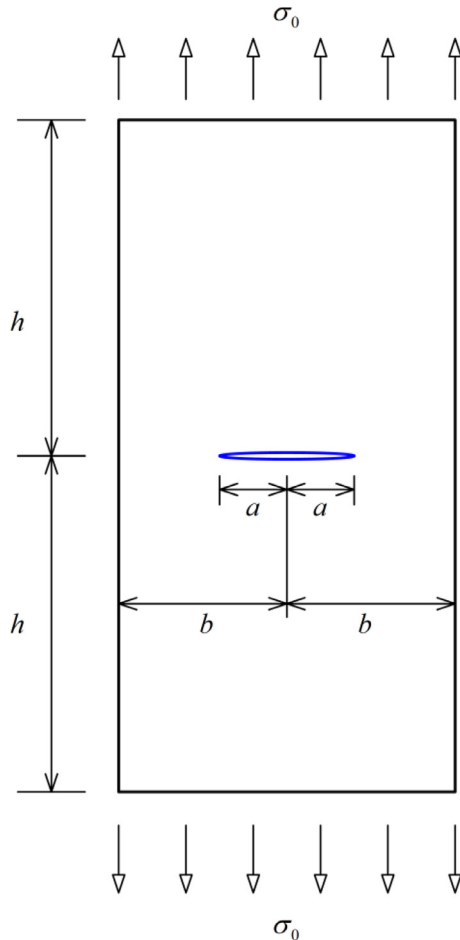


Fig. 12. The finite plate with a horizontal central crack under uniform tension.

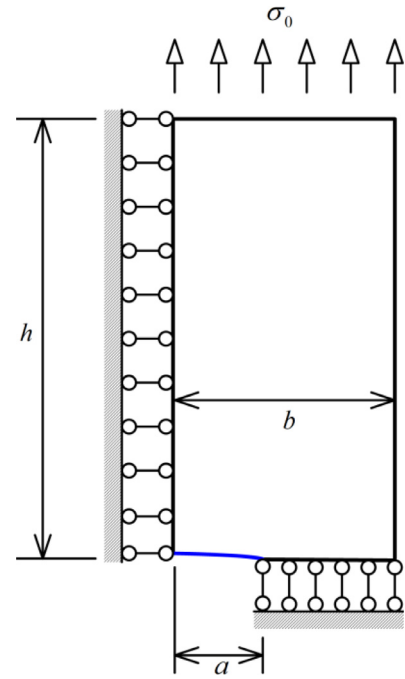


Fig. 13. Computational model for the horizontal centered cracked plate.

width and height of the plate are $2b = 200$ mm and $2h = 400$ mm, respectively. The crack length is a . The material properties of plate are Young's modulus $E = 210$ GPa and Poisson's ratio $\nu = 0.25$. Under plane stress state, the reference solution for this problem is given by Tada et al. as [39]

$$K_I^{\text{Tada}} = \sigma_0 \sqrt{\pi a} \sqrt{\sec\left(\frac{\pi a}{2b}\right)} \quad (43)$$

Owing to the symmetry, only a quarter of the plate is modeled, as displayed in Fig. 13, and the corresponding symmetric displacement constraints are applied on the two symmetrical edges.

The influence of the dimensionless parameter γ controlling the distance of source points to the element boundary is firstly considered for the case of $a = 10$ mm. The computational model in Fig. 13 is meshed by 89 hybrid elements including 6 hybrid 3-sided elements with singularity controlling and 83 general hybrid 4-sided elements, as shown in Fig. 14(a). The normalized SIF results by the present method are presented in Fig. 15, from which it is observed that the parameter γ has a large range to produce stable results. In the following computation, the parameter γ is chosen as 10, unless specifically stated.

For various crack lengths, the SIFs are obtained by the present method and listed in Table 1. All the results are computed by using 6 hybrid 3-sided singular elements to enclose the crack tip, as shown in Fig. 14. For the cases of $a = 30$ mm and $a = 50$ mm, total 57 and 56 hybrid elements are employed to model the computational domain, respectively. It is found from Table 1 that the numerical results are in good agreement with the results determined by Eq. (43).

Additionally, the computational efficiency is compared between the conventional finite element and the proposed hybrid finite element, under the condition that the same mesh division and in the same computer are used. Here, three mesh divisions, as shown in Fig. 14, are considered and the computational efficiency of each type of element is listed in Table 2, from which it is found that the present hybrid element involved boundary integrals only is slightly faster than the conventional finite element involved domain integral if the same number of Gaussian quadrature points for each local coordinate direction are employed, i.e. 3 Gaussian quadrature points are used for numerical integration along each side of the hybrid finite element, while 3 by 3 Gaussian quadrature points are used for domain integration in each conventional finite

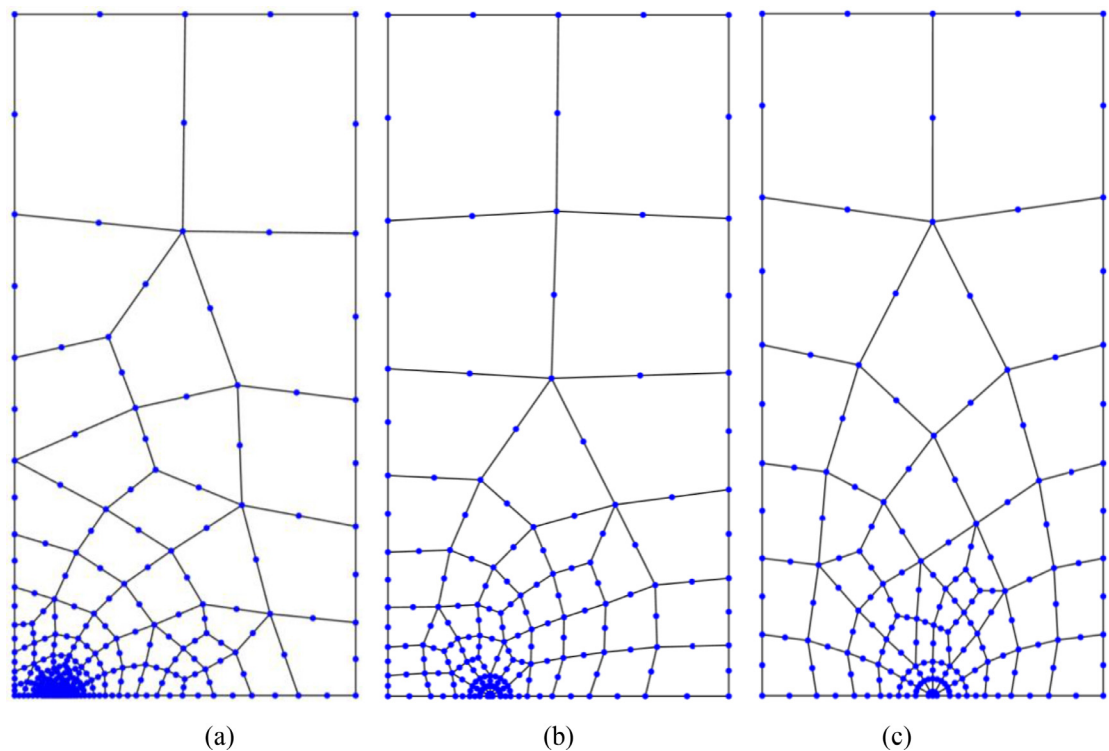


Fig. 14. Meshes used for various crack lengths for the central crack problem: (a) $a = 10$ mm, (b) $a = 30$ mm and (c) $a = 50$ mm.

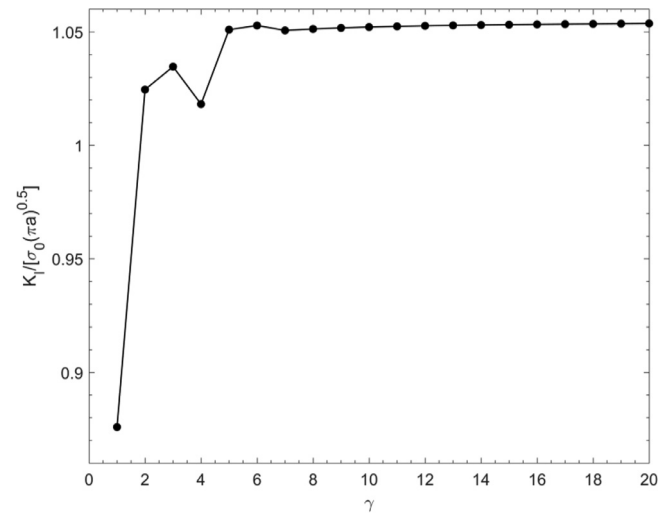


Fig. 15. Influence of the dimensionless parameter γ to the normalized SIF for the case of $a = 10$ mm.

Table 1
Normalized mode I for various crack lengths in the central-crack problem.

a/b	0.1	0.3	0.5
$K_I/(\sigma_0 \sqrt{\pi a})$	1.014	1.071	1.204
$K_I^{\text{Tada}}/(\sigma_0 \sqrt{\pi a})$	1.006	1.059	1.189

element. It is worth pointing out that the timer begins from the element loop and ends after the global stiffness matrix is assembled, because the main difference of the two types of element is the production of element stiffness matrix, as shown in Section 3.

Table 2
Comparison of computational efficiency between the present hybrid finite element and the conventional finite element.

Mesh	Hybrid finite element	Conventional finite element
Fig. 14(a)	0.090079s	0.091346s
Fig. 14(b)	0.056074s	0.057004s
Fig. 14(c)	0.054671s	0.055768s

Moreover, the accuracy and convergence of the present hybrid element is investigated through considering the case of $a = 50$ mm. In contrast to $K_I/(\sigma_0 \sqrt{\pi a}) = 1.134$ from the conventional finite element with same mesh division given in Fig. 14(c), it is found that the present hybrid finite element can give better prediction 1.204. On the other hand, 18, 41, and 56 elements with 71, 144, 189 nodes are respectively used to demonstrate the convergence of the present hybrid finite element. It is observed from Fig. 16 that the present hybrid finite element rapidly converges from 1.225 to 1.204 when the number of nodes increases from 71 to 189. The maximum relative error to the exact solution is only 3.03% produced by using 71 nodes.

Finally, different meshing strategies are discussed for illustrating the flexibility of the present hybrid finite elements. In addition to the mixed element meshing shown in Fig. 14(c), the model with $a = 50$ mm is discretized with 96 3-sided elements and 60 4-sided elements, respectively, as indicated in Fig. 17. It is found from that the normalized SIF is 1.201 for the pure 3-sided element discretization and 1.202 for the pure 4-sided element discretization. These results are very close to that from the mixed element discretization.

5.2. An inclined internal crack in a finite plate

The second example is used to test the capability of the present method for the mixed-mode loading which is achieved by a uniform

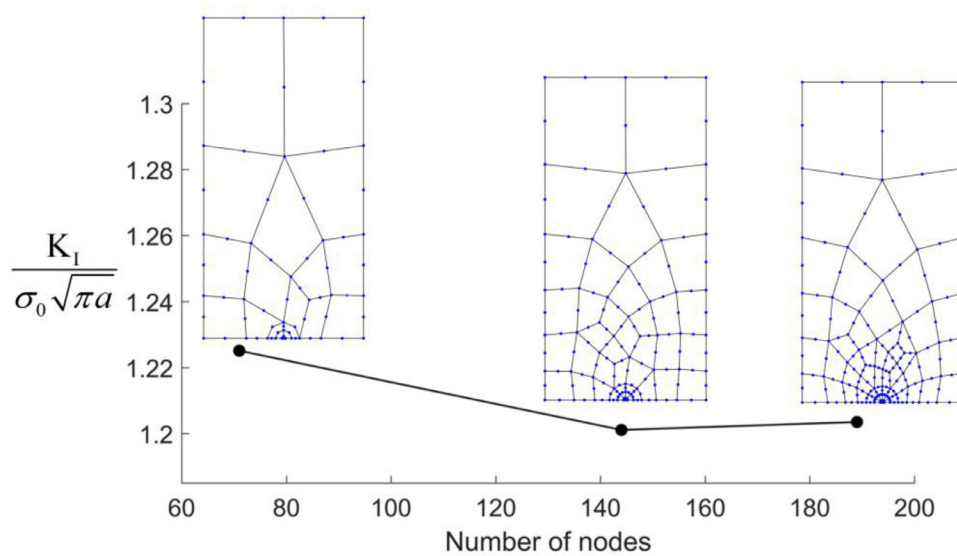


Fig. 16. Influence of the dimensionless parameter γ to the normalized SIF for the case of $a = 50$ mm.

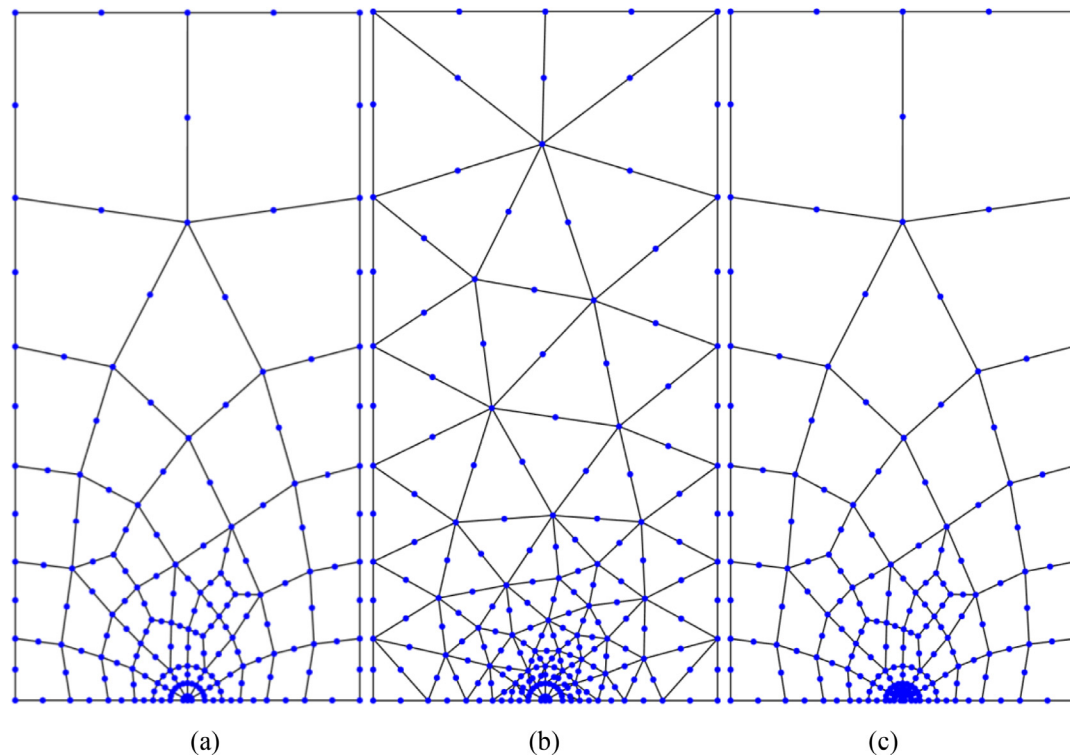


Fig. 17. Different meshing strategies for the model with $a = 50$ mm: (a) mixed element meshing, (b) 3-sided element meshing, (c) 4-sided element meshing.

tensile stress $\sigma_0 = 1$ applied at the ends of the plate with a central inclined crack, as displayed in Fig. 18. The angle of inclination is ϕ with respect to the global x_1 axis. Here, the geometric dimension of the plate is set as $2a = 1.2$, $b = 1$ and $h = 2$. The plane strain is assumed for this problem with material properties $E = 1.0$ and $\nu = 0.3$.

Fig. 19 shows the mesh configurations for various angles of inclination of crack. It is clearly seen that each crack tip is enclosed by 8 singular hybrid 3-sided elements for all computations. Additionally, 143, 145, 146 and 163 general 4-sided elements are used for the hybrid finite element simulation when the angle of inclination is 15° , 30° , 45° and 60° , respectively. The mixed-mode SIF values for various angles of inclination are listed in Table 3. The SIF results have been compared with published results from literature [40,41] using conformal mapping (CMAP) approach and super singular element method (SSEM)

respectively. The table shows that for every crack angle of inclination, good agreements on both K_I and K_{II} are observed for different solving strategies.

5.3. Two inclined internal cracks in a finite plate

Finally, a finite plate with two inclined cracks is considered, as described in Fig. 20. The geometric dimensions related to this problem are $h = 2$, $b = 1$, $a = 0.25$ and $d = 0.275$. The angle of crack inclination is $\phi = 60^\circ$. For the computational domain, the material properties are $E = 1$ and $\nu = 0.3$.

Owing to the symmetry of the domain on the middle line, only half of it is modeled, as shown in Fig. 21. Under plane strain assumption, the half-plate with one inclined crack is discretized with 16 singular

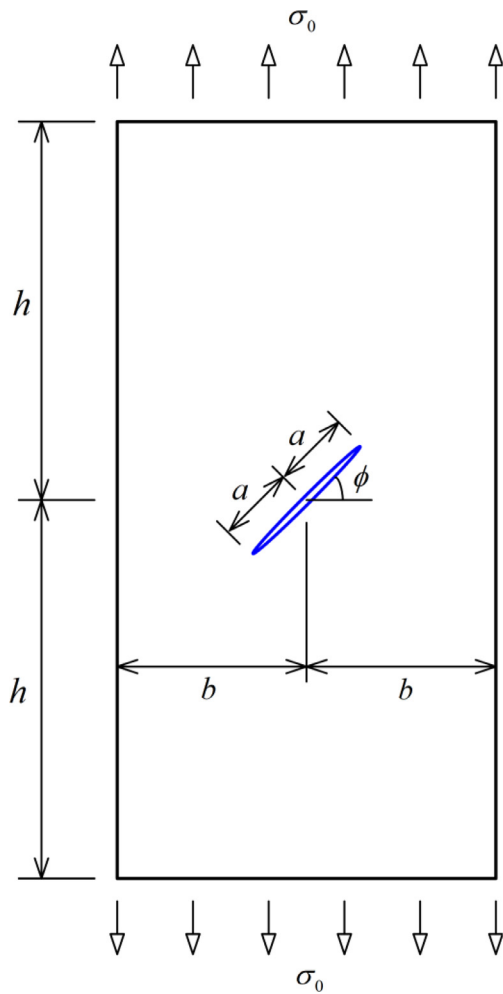


Fig. 18. The finite plate with inclined central crack under uniform tension.

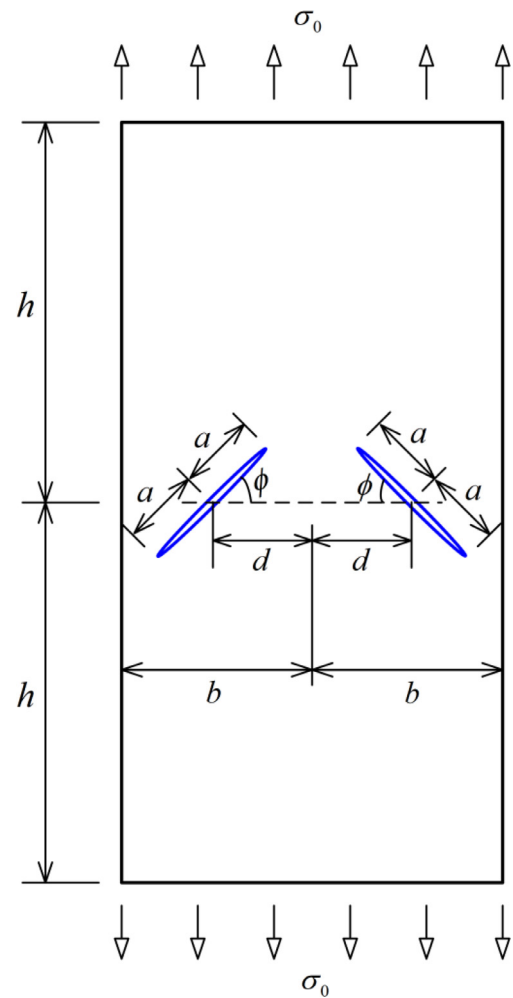


Fig. 20. The finite plate with two inclined internal cracks.

hybrid 3-sided elements enclosing the crack tips A and B. The number of general 4-sided hybrid elements are 176 and 188 for the study of $\phi = 30^\circ$ and $\phi = 45^\circ$, respectively. The mesh configurations for this two inclined angles are depicted in Fig. 22. This problem was also discussed by Chen and Chang [42], and Lu and Wu [16], and their results revealed that the SIFs are almost same for Mode I and Mode II. Thus, only the

SIF solutions of Mode I at the two crack tips A and B are discussed in this study. Table 4 compares the present SIF results with those from Chen and Chang [42], and Lu and Wu [16]. As shown in Table 4, the present results are closer to those from Lu and Wu [16]. Moreover, it is observed from the table that the SIFs become bigger as the inclination

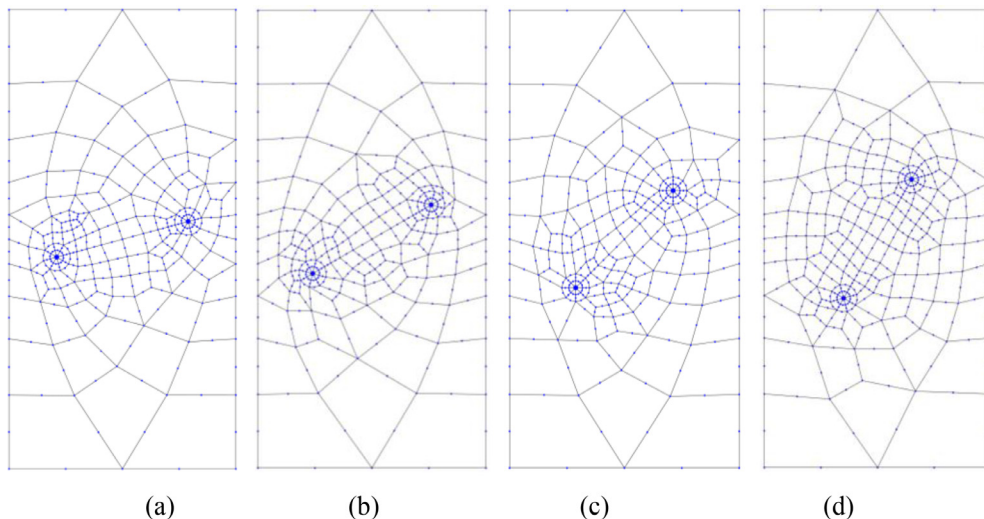


Fig. 19. Mesh configurations for various angles of inclination: (a) $\phi = 15^\circ$, (b) $\phi = 30^\circ$, (c) $\phi = 45^\circ$ and (d) $\phi = 60^\circ$.

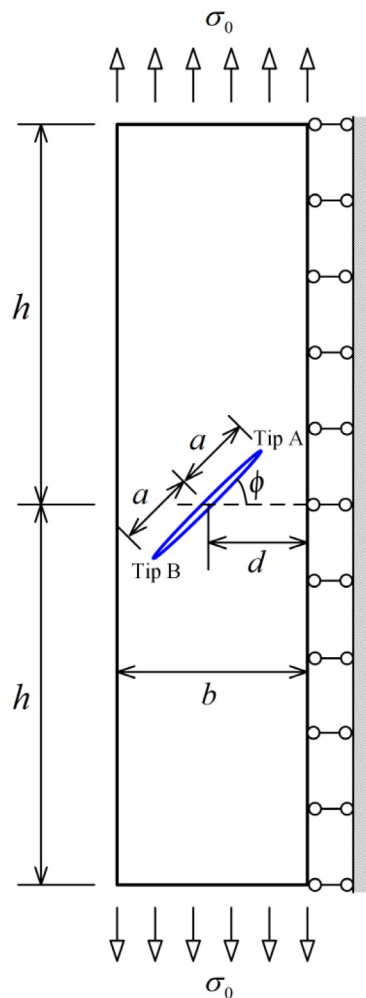


Fig. 21. The computational model of the half-plate with one inclined internal crack.

Table 3
Normalized mixed-mode SIFs for a central inclined crack under uniform tension.

ϕ	$K_I/(\sigma_0\sqrt{\pi a})$		$K_{II}/(\sigma_0\sqrt{\pi a})$	
	Present	Reference solutions [40,41]	Present	Reference solutions [40,41]
15°	1.187	1.218	0.278	0.273
30°	0.960	0.984	0.491	0.480
45°	0.646	0.661	0.581	0.567
60°	0.325	0.333	0.515	0.502

Table 4
Comparison of normalized stress intensity factor for various crack angles.

ϕ		Present	Lu and Wu [16]	Chen and Chang [42]
30°	Tip A	0.993	0.981	0.487
	Tip B	0.855	0.846	0.516
45°	Tip A	0.603	0.596	0.513
	Tip B	0.525	0.520	0.557

angle of crack becomes smaller. This can be attributed to the interaction of two cracks. The smaller the angle ϕ is, the stronger such interaction becomes.

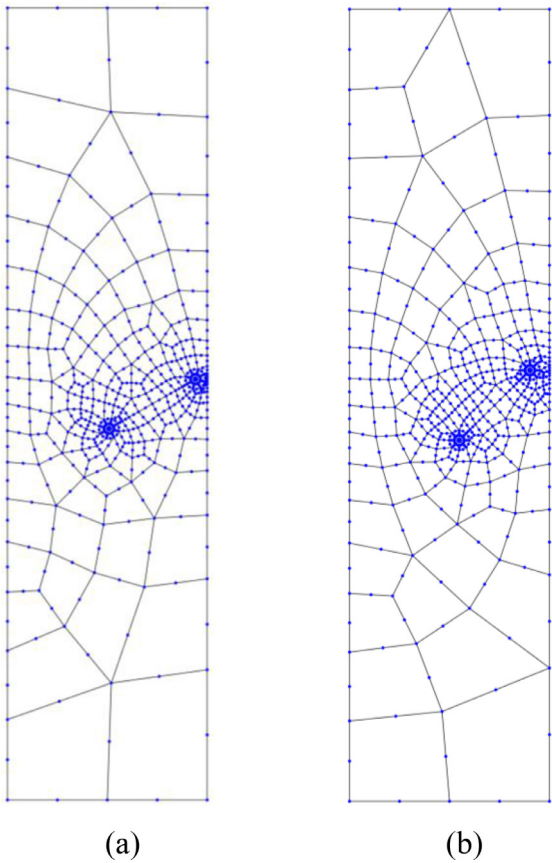


Fig. 22. Mesh configurations of the half-plate with one inclined internal crack for two angles of crack inclination: (a) $\phi = 30^\circ$ and (b) $\phi = 45^\circ$.

6. Conclusions

In this paper, the application of the hybrid finite element formulation with unified fundamental solutions as trial functions to crack problems in linear elastic medium has been investigated. The present n -sided hybrid element is in conjunction with the quarter-point singularity controlling to construct the singular hybrid elements at the crack tip, which has been proved very efficient to calculate the SIFs for mixed-mode crack problems of arbitrary geometry, as well as structures with multi-cracks. The use of discontinuous quarter-point elements at the crack tips can correctly describe the $r^{1/2}$ behavior of the near-tip displacement. Numerical results show very good agreement between the present method and published results. Further, it is demonstrated from the implementation of the present method that the present formulation can readily be incorporated into the standard FEM program framework.

Acknowledgment

This project was supported by National Natural Science Foundation of China (No. 11772204) and Program for Innovative Research Team of Science & Technology of Henan Province of China (No. 19IRTSTHN020).

References

[1] Anderson TL. Fracture mechanics: Fundamentals and applications. Boca Raton: CRC Press; 1991.
[2] Qin QH, Yu SW. An arbitrarily-oriented plane crack terminating at the interface between dissimilar piezoelectric materials. Int J Solids Struct 1997;34(5):581–90.
[3] Qin QH. Fracture mechanics of piezoelectric materials. Southampton: WIT Press; 2001.
[4] Irwin GR. Linear fracture mechanics, fracture transition, and fracture control. Eng Fract Mech 1968;1(2):241–57.

- [5] Yu S, Qin QH. Damage analysis of thermopiezoelectric properties: part II. Effective crack model. *Theor Appl Fract Mech* 1996;25(3):279–88.
- [6] Qin QH, Mai Y. Crack growth prediction of an inclined crack in a half-plane thermopiezoelectric solid. *Theor Appl Fract Mech* 1997;26(3):185–91.
- [7] Williams ML. On the stress distribution at the base of a stationary crack. *J Appl Mech* 1957;24(1):109–14.
- [8] Bathe KJ. Finite element procedures in engineering analysis. Prentice-Hall; 1982.
- [9] Qin QH. Trefftz finite element method and its applications. *Appl Mech Rev* 2005;58(5):316–37.
- [10] Brebbia CA. The boundary element method for engineers. London: Pentech Press; 1980.
- [11] Qin QH, Mai YW. BEM for crack-hole problems in thermopiezoelectric materials. *Eng Fract Mech* 2002;69(5):577–88.
- [12] Liu YJ, Li YX, Xie W. Modeling of multiple crack propagation in 2-D elastic solids by the fast multipole boundary element method. *Eng Fract Mech* 2017;172:1–16.
- [13] Barsoum RS. On the use of isoparametric finite elements in linear fracture mechanics. *Int J Numer Methods Eng* 1976;10(1):25–37.
- [14] Nikishkov GP. Accuracy of quarter-point element in modeling crack-tip fields. *CMES Comput Model Eng Sci* 2013;93(5):335–61.
- [15] Henshell RD, Shaw KG. Crack tip finite elements are unnecessary. *Int J Numer Methods Eng* 1975;9(3):495–507.
- [16] Lu XP, Wu WL. Dual boundary integral formulation for 2-D crack problems. *Commun Nonlinear Sci Numer Simul* 2010;15(6):1682–90.
- [17] Nguyen BH, Tran HD, Anitescu C, Zhuang X, Rabczuk T. An isoheometric symmetric Galerkin boundary element method for two-dimensional crack problems. *Comput Methods Appl Mech Engrg* 2016;306:252–75.
- [18] Blandford GE, Inghrafea AR, Liggett JA. Two-dimensional stress intensity factor computations using the boundary element method. *Int J Numer Methods Eng* 1981;17(3):387–404.
- [19] Wang HT, Yao ZH. A fast multipole dual boundary element method for the three-dimensional crack problems. *CMES Comput Model Eng Sci* 2011;72(2):115–47.
- [20] Wang H, Qin QH. Fundamental-solution-based hybrid fem for plane elasticity with special elements. *Comput Mech* 2011;48(5):515–28.
- [21] Qin QH, Wang H. MATLAB and C programming for Trefftz finite element methods. CRC Press; 2008.
- [22] Wang KY, Qin QH, Kang YL, Wang JS, Qu CY. A direct constraint-Trefftz FEM for analysing elastic contact problems. *Int J Numer Methods Eng* 2005;63(12):1694–718.
- [23] Qin QH. Hybrid-Trefftz finite element method for reissner plates on an elastic foundation. *Comput Methods Appl Mech Eng* 1995;122(3–4):379–92.
- [24] Qin QH. Variational formulations for TFEM of piezoelectricity. *Int J Solids Struct* 2003;40(23):6335–46.
- [25] Wang H, Qin QH. Hybrid FEM with fundamental solutions as trial functions for heat conduction simulation. *Acta Mech Solida Sin* 2009;22(5):487–98.
- [26] Qin QH. Hybrid Trefftz finite-element approach for plate bending on an elastic foundation. *Appl Math Model* 1994;18(6):334–9.
- [27] Wang H, Qin QH. Voronoi polygonal hybrid finite elements with boundary integrals for plane isotropic elastic problems. *Int J Appl Mech* 2017;9(3):1750031.
- [28] Wang H, Qin QH. n-sided polygonal hybrid finite elements with unified fundamental solution kernels for topology optimization. *Appl Math Model* 2019;66:97–117.
- [29] Wang H, Qin QH. Numerical implementation of local effects due to two-dimensional discontinuous loads using special elements based on boundary integrals. *Eng Anal Bound Elem* 2012;36(12):1733–45.
- [30] Wang H, Qin QH. Boundary integral based graded element for elastic analysis of 2D functionally graded plates. *Eur J Mech Solid* 2012;33(1):12–23.
- [31] Wang H, Zhao XJ, Wang JS. Interaction analysis of multiple coated fibers in cement composites by special n-sided interphase/fiber elements. *Compos Sci Technol* 2015;118:117–26.
- [32] Wang H, Qin QH. A meshless method for generalized linear or nonlinear Poisson-type problems. *Eng Anal Bound Elem* 2006;30(6):515–21.
- [33] Wang H, Qin QH. Fundamental-solution-based finite element model for plane orthotropic elastic bodies. *Eur J Mech Solid* 2010;29(5):801–9.
- [34] Liu GR, Quek SS. The finite element method: A practical course. 2nd ed. Butterworth-Heinemann; 2013.
- [35] Qian G, González-Albuixech VF, Niffenegger M, Giner E. Comparison of K_I calculation methods. *Eng Fract Mech* 2016;156:52–67.
- [36] Maiti SK. Fracture mechanics: fundamentals and applications. Delhi: Cambridge University Press; 2015.
- [37] Sun CT. Fracture mechanics. Academic Press; 2012.
- [38] Gray LJ, Phan AV, Paulino GH, Kaplan T. Improved quarter-point crack tip element. *Eng Fract Mech* 2003;70(2):269–83.
- [39] Tada H, Paris PC, Irwin G. The stress analysis of cracks handbook. Paris: Paris Production Inc; 1985.
- [40] Portela A, Aliabadi MH, Rooke DP. The dual boundary element method: effective implementation for crack problems. *Int J Numer Meth Eng* 1992;33(6):1269–87.
- [41] Tsang DKL, Oyadiji SO. Super singular element method for two-dimensional crack analysis. *Proc R Soc A* 2008;464(2098):2629–48.
- [42] Chen WH, Chang CS. Analysis of two-dimensional mixed-mode crack problems by finite element alternating method. *Comput Struct* 1989;33(6):1451–8.